



1 **Near real-time atmospheric and oceanic science products of Himawari-8/9**
2 **geostationary satellites over the South China Sea**

3
4 Jian Liu¹, Jingjing Yu¹, Chuyong Lin¹, Min He¹, Haiyan Liu¹, Wei Wang², Min Min^{2*}

5
6
7 ¹ School of Geography and Ocean Science, Ministry of Education Key Laboratory for Coast
8 and Island Development, Nanjing University, Nanjing 210023, China, and Southern Marine
9 Science and Engineering Guangdong Laboratory (Zhuhai), Zhuhai 519082, China

10 ² School of Atmospheric Sciences and Guangdong Province Key Laboratory for Climate
11 Change and Natural Disaster Studies, Sun Yat-sen University, Zhuhai 519082, China

12
13
14
15
16
17
18 *Corresponding author: minm5@mail.sysu.edu.cn

19
20
21
22
23
24
25
26



27

Abstract

28 The initial release of near real-time (NRT) atmospheric and oceanic science products from
29 Japanese Himawari-8/9 (H8/9) geostationary (GEO) satellites over the South China Sea (SCS)
30 was unveiled in 2024. The primary objective behind crafting these NRT H8/9 satellite products
31 is to facilitate weather and marine environment monitoring, enhance maritime security, and aid
32 ocean navigation, among other purposes. As part of this investigation, a novel NRT data
33 processing system was devised to generate a variety of regional H8/9 GEO satellite science
34 products within a temporal resolution of 10 minutes and a gridded resolution of $0.05^\circ \times 0.05^\circ$
35 from November 3, 2022 to the present. This algorithm system was built upon the preceding
36 FengYun (FY) geostationary satellite algorithm testbed (FYGAT), which was the prototype of
37 FY-4 GEO meteorological satellite science product operational processing system. These
38 regional H8/9 GEO satellite science products encompass a range of crucial data such as cloud
39 mask, fraction, height, phase, optical and microphysical properties, layered precipitable water,
40 sea surface temperature, etc. We subjected these products to rigorous evaluations against high-
41 quality analogous satellite products and reanalysis data spanning four months in 2023. The
42 validations underscore a strong consistency between the H8/9 GEO satellite atmospheric and
43 oceanic science products over the SCS and the referenced products. Nevertheless, slight
44 discrepancies in these satellite science products were identified, primarily stemming from
45 variations in sensor/dataset characteristics, retrieval algorithms, and geometric conditions.
46 These outcomes demonstrate the suitability of the first edition of NRT atmospheric and oceanic
47 science products of H8/9 satellites over the SCS in supporting the intended quantitative
48 applications. This NRT GEO satellite data record is publicly accessible through the File
49 Transfer Protocol (FTP) provided by the Southern Marine Science and Engineering Guangdong
50 Laboratory (Zhuhai) in China. Free access to the dataset can be found at
51 <https://doi.org/10.6084/m9.figshare.25015853> (Liu, 2024).

52

53 **Keywords:** Cloud; Geostationary Satellite; South China Sea; Layered Precipitable Water; Sea
54 surface temperature.

55

56



57 **1 Introduction**

58 The South China Sea is located to the south of mainland China and in the western
59 Pacific Ocean. It stands as the largest and deepest sea area in China, boasting an average
60 depth of 1212 meters and reaching a maximum depth of 5559 meters. Due to its
61 proximity to the equator, the SCS receives a substantial amount of solar radiation,
62 resulting in high local temperatures and humidity. The regional annual average air
63 temperature ranges from 25°C to 28°C. Even during the coldest months, the average
64 temperatures remain above 20°C, while extreme high-temperature events can reach
65 about 33°C. The average sea surface temperature (SST) in the SCS is around 26°C, and
66 the seasonal variation is not significant. Furthermore, the South China Sea and the
67 Western Pacific serve as abundant sources of water vapor, leading to considerable
68 precipitation in the SCS. Typhoon-related rainfall accounts for about one-third of the
69 total rainfall in the region. On average, the SCS experiences over 1300 mm of rainfall
70 annually, with the majority concentrated in the summer half-year (Ding and Liu, 2001;
71 Wang et al., 2009; Wang et al., 2011).

72 The SCS region also experiences a distinct tropical maritime monsoon climate.
73 After October of each year, winter air currents originating from Siberia and the
74 Mongolian Plateau consistently flow towards the SCS (Martin and Howland, 1982). As
75 a result, from November to March of the following year, the SCS region is dominated
76 by the northeast monsoon. Starting in April, the SCS is influenced by tropical and
77 equatorial ocean air masses, inducing the prevalence of the southwest monsoon from
78 May to September. Besides, the SCS is often affected by typhoons during the summer
79 and autumn seasons. About 70% of these typhoons originate from the Western Pacific,
80 east of the Philippines, and the vicinity of the Caroline Islands, while the remaining 30%
81 are generated locally from the sea areas near the Xisha and Zhongsha Islands in the
82 SCS (Ding and Liu, 2001; Jiang et al., 2023; Niu and Feng, 2021; Wang et al., 2020).

83 On account of lack of ground-based observations over the SCS, satellites,
84 particularly geostationary (GEO) meteorological satellites, have emerged as the most
85 effective means of observing weather patterns, climate, and environmental changes in
86 oceanic regions. For instance, satellite-based rain rate, SST, outgoing longwave
87 radiation (ORL), convective clouds, etc. are commonly used for examine the summer
88 monsoon, marine heatwave, rainfall, and convection over the SCS (Koseki et al., 2013;
89 Li et al., 2022b; Liu et al., 2014; Xu et al., 2021; Zhou et al., 2024). In recent years,
90 countries across the world, such as China, U.S., Japan, and Korea, have made their own



91 remarkable progress in the development of next-generation geostationary
92 meteorological satellites. Enhanced imaging capabilities in spectral, temporal, and
93 spatial resolutions of the next-generation GEO meteorological satellite allows for more
94 detailed and accurate observations of cloud formations, atmospheric conditions, and
95 natural disasters like hurricanes and typhoons, such as Fengyun-4A/B (FY-4) operated
96 by the China Meteorological Administration (CMA) and Himawari-8/9 (H8/9)
97 satellites operated by the Japan Meteorological Agency (JMA) (Husi et al., 2019; Kim
98 et al., 2021; Schmit et al., 2017; Yang et al., 2017). Expect to GEO advanced imager,
99 many nations have equipped their geostationary lightning and infrared hyperspectral
100 sounder detection sensors to track and analyze thunderstorms, lightning activity,
101 atmospheric temperature and humidity profile, and even wind field in real-time (Li et
102 al., 2022a; Ma et al., 2021; Min et al., 2017b).

103 Although the JAXA (Japan Aerospace Exploration Agency) official FTP site
104 (<ftp.ptree.jaxa.jp>) has already offered the freely download links of some H8/9 Level-2
105 (L2) science products, such as cloud phase and optical depth (Husi et al., 2019), from
106 July 7 of 2015 to present with approximate two hours lag, the relatively low timeliness
107 and lack of variety of operational satellite science products have seriously affected the
108 data quantitative applications in weather and marine environment monitoring over the
109 SCS. Particularly, time-delayed GEO satellite products cannot be utilized in maritime
110 security and navigation fields, which are of vital importance as it ensures the safety of
111 crew members, transportation of goods, protection of the marine environment, etc.
112 (Soldi et al., 2021). However, as recommended by the JMA, the near real-time down-
113 sampling full-disk H8/9 Level-1B (L1B) radiance data (including 14 bands with
114 horizontal resolutions of 1 km (visible, VIS) and 4 km (near infrared and infrared, NIR
115 and IR bands), and excluding two VIS bands at 0.47 μm and 0.51 μm) are able to be
116 received by using the compact and exclusive geostationary satellite data receiving
117 antenna from the JMA Himawari-Cast (Wang et al., 2019; Xia et al., 2023). Therefore,
118 based on the received real-time H8/9 full-disk L1B data, the primary goal of this
119 investigation is to develop several NRT L2 Atmospheric and Oceanic science products
120 over the SCS (abbreviated as NANO_SCS) that are released online. It is the first edition
121 of the NRT H8/9 GEO satellite science products generated by the NANO_SCS system.
122 The next sections will be devoted to the introduction and validation of these NRT H8/9
123 GEO satellite scientific products. Both the NANO_SCS satellite data processing and



124 management systems are operated by the Southern Marine Science and Engineering
125 Guangdong Laboratory (Zhuhai) of China.

126 The subsequent sections of this study are meticulously organized as follows.
127 Section 2 briefly introduces the Himawari-8/9 satellites, elucidating the intricate details
128 of the main processing or production flow, as well as shedding light on the remarkable
129 NRT science products specifically tailored for the South China Sea region. In Section
130 3, it shows some sample results and verifies the key science products, ensuring their
131 accuracy and reliability. Section 4 elucidates data download method. Finally, in Section
132 5, we summarize the main conclusions of this study, while also outlining our future
133 vision plans for further enhancing and expanding the scope of the NANO_SCS dataset.
134

135 **2 Data production**

136 *2.1 Data*

137 The Himawari-8/9 satellites, which are the new-generation and state-of-the-art
138 GEO meteorological satellites operated by the JMA, were successfully launched on
139 October 7, 2014, and November 2, 2016, respectively. These advanced satellites
140 operate in a highly sophisticated three-axis stabilized mode, ensuring high spatial-
141 temporal, precise and stable observations. It is worth highlighting that on December 13,
142 2022, at 05:00 UTC, the H9 GEO meteorological satellite seamlessly replaced its
143 predecessor, the H8 GEO satellite, marking a significant milestone in GEO satellite
144 operations (<https://www.data.jma.go.jp/mscweb/en/index.html>). This strategic location
145 allows for comprehensive full-disk observation mode, enabling the satellites to capture
146 detailed imagery of the entire Earth's disk, with a particular focus on the Japanese island
147 and its surrounding areas. The Advanced Himawari Imager (AHI), as a unique and
148 highly advanced optical sensor designed specifically for earth viewing, has 16
149 independent earth-view bands, covering an extensive range of wavelengths from 0.45
150 to 13.3 μm . These bands include three visible (VIS) bands, three near-infrared (NIR)
151 bands, and ten infrared (IR) bands, each serving a specific purpose in capturing and
152 analyzing various aspects of the Earth's atmosphere and surface. The AHI routinely
153 operates in two observation modes: a full-disk observation mode that captures full disk
154 images within a 10-minute time interval, and a fast regional scanning mode that allows
155 for swift maneuvering and scanning within a 2.5-minute interval. This regional
156 scanning mode is particularly useful for capturing high-resolution imagery of specific



157 regions of interest, enabling detailed analysis and examination of localized weather
158 events. The nominal spatial resolutions of the H8/9-AHI sensor vary depending on the
159 specific band being utilized. For the VIS band at 0.65 μm , the spatial resolution is 0.5
160 km. The NIR bands have a spatial resolution of 1 km, while the IR bands have a spatial
161 resolution of 2 km (Bessho et al., 2016; Husi et al., 2019; Letu et al., 2020; Min et al.,
162 2019). In this study, we only used the down-sampling H8/9 L1B radiance data
163 mentioned before to product NRT dataset. The spatial resolution for the down-sampling
164 VIS band at 0.65 μm was reduced to 1.0 km, while the other bands were down-sampled
165 to 4.0 km. The scope of this investigation covers the South China Sea region,
166 specifically from 0° to 40°N latitude and 100°E to 140°E longitude. The utilization of
167 IR bands with a spatial resolution of 4.0 km limits the related L2 satellite science
168 products to the same resolution. Therefore, based on the products with the spatial
169 resolution of 4.0 km, the final regional L2 atmospheric and oceanic science products
170 are analyzed and projected into a user-friendly gridded resolution of $0.05^\circ \times 0.05^\circ$.

171 The NRT GEO satellite retrieval system (or NANO_SCS system) developed in
172 this study also utilizes the high-resolution operational numerical weather prediction
173 (NWP) data as ancillary data from the Global Forecast System (GFS), which boasts a
174 gridded horizontal resolution of $0.25^\circ \times 0.25^\circ$ and encompasses a 41 vertical layers
175 ranging from 1000 to 0.01 hPa within a 3-hour time interval. The GFS NWP data can
176 be effortlessly accessed and downloaded from the National Oceanic and Atmospheric
177 Administration (NOAA) website
178 (<https://nomads.ncep.noaa.gov/pub/data/nccf/com/gfs/prod>) at four distinct initial
179 forecast times (00_00, 06_00, 12_00, and 18_00 UTC). To ensure optimal efficiency
180 for the operations of subsequent day, only 9 continuous data (ranging from 018, 021,
181 024, ... to 042) generated at a fixed initial forecast time of UTC 06_00 are selectively
182 downloaded within a predefined time period each day (Whitaker et al., 2008).

183 We collect and use four months (January, April, July, and October of 2023) Climate
184 Data Records (CDR) from the latest MODIS (Moderate Resolution Imaging
185 Spectroradiometer) Collection-6.1 Level-2 cloud, land surface temperature (LST), and
186 sea surface temperature (SST) products to validate the NRT H8/9 GEO satellite science
187 products (Platnick et al., 2003; Platnick et al., 2017). MODIS, as a key optical sensor
188 aboard NASA's Terra and Aqua polar-orbiting satellites since 1999 and 2002, can
189 provide high resolution (1.0 km) L2 science products about the Earth's surface and
190 atmosphere (<https://search.earthdata.nasa.gov/search>). MODIS data are freely available



191 to the public and are widely used by scientists, government agencies, and researchers
192 around the world, which are always used to verify the other congeneric satellite
193 products (Min et al., 2020). Furthermore, we also compare the NRT layered
194 precipitable water (LPW) product over the SCS with matched ERA5 reanalysis data
195 (the fifth-generation European Center for Medium Range Weather Forecasts
196 Reanalysis data) (Hersbach et al., 2020). The hourly layered specific humidity data for
197 the same four months (January, April, July, and October of 2023) with a horizontal
198 resolution of $0.25^{\circ} \times 0.25^{\circ}$ have been downloaded freely from the ERA5 dataset. This
199 data will be employed for the validation of the layered precipitable water product of
200 H8/9 GEO satellite. You can access the data at
201 <https://cds.climate.copernicus.eu/cdsapp#!/home>.

202

203 *2.2 NRT processing flow and science products*

204 As extensively discussed in the former study by (Min et al., 2017b), significant
205 strides were made in the development of the operational prototypes of FY-4 GEO
206 satellite science product algorithms. These remarkable advancements were achieved
207 through the collaborative efforts of the scientists in the FY-4 GEO satellite Algorithm
208 Working Group (AWG) in China, who successfully developed two highly robust
209 Fengyun science product algorithm testbeds (or FYGAT) specifically tailored for
210 imagers and sounders. For a comprehensive understanding of the intricate details of
211 FYGAT, interested readers are strongly encouraged to refer to the aforementioned
212 literature written by (Min et al., 2017b). The FYGAT for imager is the key module of
213 the NANO_SCS system for rapidly retrieve the first edition of NRT L2 science
214 products of H8/9 GEO satellites.

215 Figure 1 shows the comprehensive NRT processing flowchart of the NANO_SCS
216 system. The dark gray shading cylinder icons in the figure represent the key processing
217 modules of the system, including retrieval, projection, and drawing modules. Following
218 the synthesis of NRT satellite data, the retrieval module initially retrieves the cloud
219 mask product to identify clear and cloudy sky pixels within the targeted SCS region.
220 Then, for cloudy-sky pixels, he retrieval module sequentially executes algorithms for
221 retrieving cloud fraction, cloud type/phase, cloud top properties, cloud optical and
222 microphysical properties, and cloud base properties products. However. the accurate
223 retrieval of science products from previous algorithms is crucial for the successful
224 execution of subsequent backend algorithms. For instance, the cloud optical and



225 microphysical properties algorithm relies on inputs such as cloud phase and top
226 properties to determine specific ice/water cloud optical and radiative properties lookup
227 tables (LUT) and atmospheric correction methods above the cloud (Platnick et al., 2017;
228 Walther et al., 2011) used in retrieval procedure. In a stark contrast, other science
229 algorithms for clear-sky pixels can be executed in parallel as they are independent of
230 each other, such as the algorithms for land surface temperature (LST) and sea surface
231 temperature (SST). It is important to note that due to retrieval efficiency and computing
232 resource limitations, the physics-based layered precipitable water (LPW) algorithm
233 (Zhu et al., 2023) is executed only once every half an hour.

234 Table 1 provides a list of the main NRT H8/9 GEO satellite atmospheric and
235 oceanic science products in the first edition, along with their corresponding variables,
236 generated by the NANO_SCS system from 3 November 2022 to the present. It includes
237 the variable name, valid value, and corresponding notes of satellite science products.
238 These products are stored in the Hierarchical Data Format-5 (HDF5) format within a
239 10-minute interval. The NRT GEO satellite science product is typically referred to as
240 "AH19_L2_CLM_20230815_0650_4000M_proj.HDF5". In this naming convention,
241 the abbreviation of "CLM" stands for Cloud Mask (all abbreviations are three
242 characters long), while "20230815_0650" denotes the specific observation time of the
243 satellite data, including year, month, day, hour, and minute. Lastly, "4000M_proj"
244 indicates the spatial resolution of 4000 meters and projected data. Certain related
245 variables, such as cloud top temperature, pressure, and height, are stored in the same
246 HDF5 format GEO satellite science product file, specifically the CTP (Cloud Top
247 Properties) product file (refer to Table 1).

248 Figure 2 displays the quick view images of cloud top height, cloud mask, cloud
249 base height, and cloud optical depth at 03:00 UTC on July 31, 2023, as well as
250 atmospheric total precipitable water (from LPW product) and SST retrieved at clear-
251 sky pixels at 10:00 UTC on August 15, 2023, over the SCS. These NRT product images
252 are obtained from the NANO_SCS system. The four cloud product subfigures from
253 July 31, 2023, capture the presence of Super Typhoon "Khanun" (its international
254 number: 2306), which originated in the southwestern waters of Guam on July 22, 2023.
255 It has been observed that the cloud system of Super Typhoon "Khanun" can reach
256 maximum cloud top heights exceeding 16 km and minimum cloud base height lower
257 than 1 km. The productions of all the NRT satellite science products and quick view
258 images of the NANO_SCS system are typically delayed by approximately 17 minutes



259 from the observation time. Besides, a user-friendly quick-view website
260 (<http://meteorsatellite.hellosea.org.cn/#/index>) has been created to provide users with a
261 convenient way to access and monitor the NRT H8/9 satellite data over the SCS.

262

263 **3. Results and validations**

264 *3.1 Cloud mask and fraction*

265 To differentiate between clear-sky and cloudy pixels in satellite earth-view image,
266 the cloud mask (CLM) product is firstly retrieved by the NANO_SCS system (refer to
267 Figure 1). It serves as a fundamental and primary L2 scientific output of GEO satellite
268 imaging sensors, playing a crucial role in generating high-quality subsequent satellite
269 products. As mentioned in the previous studies (Heidinger et al., 2012; Liang et al.,
270 2023; Wang et al., 2019), we used the new unified cloud mask algorithm (Wang et al.,
271 2019) of early development to retrieve and generate H8/9 CLM product firstly.
272 Utilizing the 0.64, 1.61, 3.88, 7.3, 11.2, and 12.3 μm channels of H8/9-AHI, the CLM
273 algorithm on this GEO satellite will perform 13 distinct cloud/clear-sky tests. These
274 tests are categorized into four groups: solar reflectance (SolRef), infrared (IR),
275 shortwave infrared (SWIR), and spatial uniformity tests (Wang et al., 2019; Xia et al.,
276 2024).

277 After successfully retrieving the cloud mask product, similar to the MODIS
278 algorithm (Zhao and Girolamo, 2006), cloud fraction (CLF) is calculated in a down-
279 sampled 5×5 neighboring pixel box as follows:

$$280 \text{Cloud Fraction} = 100\% \times (A + B) / (5 \times 5), \quad (1)$$

281 where A and B represent the total numbers of cloudy and probably cloudy pixels in the
282 same 5×5 neighboring pixel box, respectively. It is noting that the cloud fraction
283 product is also projected into a user-friendly gridded resolution of $0.05^\circ \times 0.05^\circ$. More
284 descriptions on these two products can be found in Table 1.

285 A pixel-to-pixel validation was performed on the H8/9 satellite CLM product over
286 the SCS using four months of MODIS data from the NANO_SCS system. To
287 quantitatively assess the quality of the GEO satellite CLM product, we employed four
288 significant scores: the probability of detection (POD) or recall rate, the false-alarm ratio
289 (FAR), the hit rate (HR) or accuracy, and the Kuiper's skill score (KSS). These metrics
290 were divided into PODcld, PODclr, FARcld, and FARclr, indicating clear and cloudy
291 pixels respectively. For detailed equations and meanings, please refer to previous
292 literature (Wang et al., 2019). In Figure 3a~3d, we present two cloud mask comparison



293 samples between H9/AHI GEO satellite and MODIS at 05:10 and 17:20 UTC on
294 January 8, 2023. It is evident that the CLM results from H9/AHI align well with the
295 latest MODIS official products across both land and sea. Additionally, Figure 3e
296 displays the POD, FAR, HR, and KSS scores of H9/AHI results for all matched pixels
297 over land and ocean. Notably, both PODcld and HR exceed 0.90, consistent with our
298 prior study (Wang et al., 2019), indicating a relatively high-quality CLM product.
299 Moreover, considering that cloud fraction depends on the cloud mask product (refer to
300 Eq. (1)), we opted against using similar products for verification in this analysis.

301

302 *3.2 Cloud type and phase*

303 Cloud type and phase as thermodynamics characteristics signify the state of water
304 vapor and minuscule particles within the cloud. It plays a critical role in weather and
305 climate research as different cloud phases influence the reflection and absorption of
306 solar radiation, consequently impacting Earth's energy balance and climate change
307 (Mülmenstädt et al., 2021). Due to the similarities in detection channels (using 7.3, 8.5,
308 11.2, and 12.3 μm channels), the cloud type and phase (CLP) retrieval algorithm
309 developed here for H8/9-AHI was based on the corresponding algorithm used for U.S.
310 new-generation Geostationary Operational Environmental Satellites (GOES-R)
311 (Pavolonis, 2010b; Pavolonis et al., 2005). The physical foundation of this algorithm is
312 the radiative transfer equation or forward model for cloudy sky at a specific infrared
313 wavelength λ , which can be expressed as follows (Min et al., 2020):

$$314 I_{obs}(\lambda) = \varepsilon(\lambda)I_{ac}(\lambda) + \varepsilon(\lambda)T_{ac}(\lambda)B(\lambda, t_{eff}) + I_{clr}(\lambda)[1 - \varepsilon(\lambda)], \quad (2)$$

315 where I_{obs} is the observed radiance, I_{clr} is the clear-sky radiance, and I_{ac} is the above-
316 cloud upwelling atmospheric radiance, respectively. I_{clr} can be precisely simulated by
317 the coupled fast IR radiative transfer model in the FYGAT system with the input of
318 matched GFS NWP data. ε and T_{ac} respectively represent the cloud emissivity and
319 above-cloud transmittance. B and t_{eff} are the Planck function and the cloud effective
320 temperature, respectively.

321 From Eq. (2), a pair of effective cloud emissivity from two different channels can
322 be used to calculate the ratio of effective absorption optical thickness τ_{abs} of cloud,
323 which is known as the beta ratio (β) and written as follows (Heidinger and Pavolonis,
324 2009; Parol et al., 1991):

$$325 \beta_{obs} = \frac{\ln[1-\varepsilon(\lambda_1)]}{\ln[1-\varepsilon(\lambda_2)]} = \frac{\tau_{abs}(\lambda_1)}{\tau_{abs}(\lambda_2)}, \quad (3)$$



326 Actually, this parameter represents the ratio of the effective absorption optical depth at
327 two different channels or wavelengths. it can describe β_{obs} by utilizing the computed
328 single scattering properties of cloud particles, along with a given cloud particle size
329 distribution and optical properties. (Parol et al., 1991). The β_{theory} can be expressed as
330 follows:

$$331 \quad \beta_{theory} = \frac{[1-\omega(\lambda_1)g(\lambda_1)]\alpha_{ext}(\lambda_1)}{[1-\omega(\lambda_2)g(\lambda_2)]\alpha_{ext}(\lambda_2)}, \quad (4)$$

332 where ω , g , and α_{ext} are the single scattering albedo, asymmetry parameter, and
333 extinction cross section, respectively. Considering the weak impact of multiple
334 scattering, Parol et al., (1991) demonstrated the a good approximation of $\beta_{theory} \approx \beta_{obs}$ in
335 the range of 8~15 μm . Eq. (4) is independent of satellite observed radiance, cloud
336 altitude, or cloud optical thickness. By using β ratio instead of brightness temperature
337 difference (BTD), it not only consider the contribution of clear-sky conditions to
338 radiation but also provide a method to link observations with theoretical cloud particle
339 distribution and optical properties.

340 Based on the differences in β ratios (i.e. $\beta[8.5/11.2\mu\text{m}]$, $\beta[12.3/11.2\mu\text{m}]$, and
341 $\beta[7.3/11.2\mu\text{m}]$) between ice and water clouds, this algorithm effectively identifies cloud
342 type and phase by integrating cloud emissivity ϵ with observed brightness temperature.
343 More details of this algorithm can be found from the previous literatures (Pavolonis,
344 2010a; Pavolonis, 2010b). The six specific cloud types of this CLP product include
345 liquid water (cloud top temperature > 273K), supercooled water (liquid water clouds
346 with cloud top temperature < 273K), mixed (which encompass both ice and water
347 clouds), optically thick ice, optically thin ice, and multilayered ice clouds. The cloud
348 phase product can be defined by summarizing the first three types of clouds and ice
349 phase clouds using the last three different ice clouds (see Table 1).

350 Figure 4 illustrates the cloud phase comparisons between the H9/AHI GEO
351 satellite and MODIS at 05:10 UTC on January 8, 2023, and 04:30 UTC on July 10,
352 2023. This comparison reveals consistent results between the two products. Notably, in
353 Figures 4a and 4c, the new H9/AHI cloud phase product identifies some newly added
354 mixed-phase cloud targets, a feature lacking in the MODIS official cloud phase product
355 (King et al., 1997). However, despite this addition, the distribution pattern of cloud
356 phases remains consistent between the two products as depicted in Figure 4. The POD)
357 and FAR for ice and water clouds (Lai et al., 2019) are 0.94/0.15 and 0.70/0.13,
358 respectively.



359

360 3.3 Cloud top and base properties

361 Cloud geometry thickness (CGT), including top and base heights (CTP and CBP),
362 enables the profiling of the vertical structure of clouds, which is vital for understanding
363 global weather and climate systems (Viúdez-Mora et al., 2015; Wang et al., 2022).
364 Using the same beta ratio (β) theory discussed in Section 3.2, the optimal estimation
365 (OE) method (Rodgers, 2000), and observed brightness temperatures (BT) at 11.2, 12.3,
366 and 13.3 μm channels, a classical one-dimensional variational (1DVAR) algorithm
367 applies a cost function ζ (refer to Eq. 5) to estimate the cloud top temperature (CTT),
368 which can be written as follows :

$$369 \zeta = [x - x_a]^T Cov_a^{-1} [x - x_a] + [y - M(x)]^T Cov_y^{-1} [y - M(x)], \quad (5)$$

370 where x , y , x_a , $M(x)$, Cov_a , and Cov_y , represent the posterior state vectors, the
371 observation vectors (include $BT_{11\mu\text{m}}$, $BTD_{11-12\mu\text{m}}$, and $BTD_{11-13.3\mu\text{m}}$), the priori state or
372 first guessed vectors (include CTT, cloud emissivity ε at $11\mu\text{m}$, and $\beta[12/11\mu\text{m}]$), the
373 forward radiative transfer model (based on Eq. (2) in the CTP retrieval algorithm), and
374 the error covariance matrices of the priori state vectors (x_a) and the differences between
375 observations and the forward radiative transfer model of $M(x)$, respectively. As a
376 nonlinear least squares fitting problem, the classical Levenberg-Marquardt iteration
377 method is used here to minimize the cost function of ζ , which can be written as follows
378 (Levenberg, 1944):

$$379 \delta x = (Cov_a^{-1} + K^T Cov_y^{-1} K)^{-1} (K^T (Cov_y^{-1} [y - M(x)]) + Cov_a^{-1} [x_a - x]), \quad (6)$$

380 where K signifies the Jacobi or Kernel matrix. The optimal values of CTT, cloud
381 emissivity, and $\beta[12/11\mu\text{m}]$ will be obtained when the iteration converges the satellite
382 observation vectors of y . It is worth noting that the beta ratio (β) plays a specific role in
383 this retrieval algorithm by analytically solving equations in the Jacobi matrix stated in
384 Eq. (6), thereby resulting in a significant enhancement of operational processing
385 efficiency. After obtaining the optimal CTT, the matched GFS-NWP temperature
386 profile is utilized to interpolate the corresponding cloud top height and pressure. For
387 more detailed information on the CTP retrieval algorithm of H8/9-AHI, please refer to
388 the study from Min et al., 2020.

389 In contrast, the successful retrieval of cloud base properties requires more inputs
390 such as cloud mask, type, top height, and optical and microphysical properties (convert
391 to cloud water path, CWP, unit = g/m^2) as discussed in Sections 3.1, 3.2, and 3.4. Wang



392 et al. (2023) have recently developed and improved a new CBP retrieval algorithm for
393 GEO H8/9-AHI, which refers to the CLAVR-x cloud base properties algorithm (Clouds
394 from AVHRR Extended, NOAA's operational cloud processing system for the AVHRR)
395 (Noh et al., 2017; Wang et al., 2024). This algorithm can only be executed during the
396 daytime (solar zenith angle $< 65^\circ$) because it relies on cloud top height (CTH) and cloud
397 water path to calculate the two linear fitting coefficients, namely slope (A_1) and
398 intercept (A_2) (Noh et al., 2017). These two coefficients are determined through
399 piecewise fitting using the CTH, CWP, and cloud base height (CBH) data obtained
400 from the joint CloudSat/CALIPSO (Cloud-Aerosol Lidar and Infrared Pathfinder
401 Satellite Observation) product (Noh et al., 2017). Once the two corresponding fitting
402 coefficients are obtained, the cloud geometric thickness can be calculated as follows:

$$403 \quad CGT = A_1 \times CWP + A_2, \quad (7)$$

404 After that, the CBH can be easily calculated using the formula $CBH = CTH - CGT$.

405 Previous studies have validated the CTH and CBH products obtained through the
406 same algorithms used for the H8 satellite, leveraging joint CloudSat/CALIPSO product
407 (Min et al., 2020; Min et al., 2017b; Wang et al., 2022; Wang et al., 2024). The mean
408 absolute error (MAE) and standard deviation (STD) for GEO satellite CTH are reported
409 as 3.18 km and 3.75 km, respectively, with a noticeable increase associated with higher
410 CTH values. Additionally, the MAE and root-mean-square error (RMSE) for CBH,
411 retrieved by the same GEO CLAVR-x algorithm, stand at 1.938 km and 2.91 km, as
412 reported in prior studies (Min et al., 2020; Wang et al., 2024). In Figure 5, CTH
413 comparisons between the H9/AHI GEO satellite and MODIS are presented for 18:50
414 UTC on October 8, 2023, and 04:30 UTC on July 10, 2023. The figure well
415 demonstrates consistent CTH values and horizontal distributions derived from both
416 H9/AHI and MODIS datasets.

417

418 *3.4 Cloud optical and microphysical properties*

419 The cloud optical thickness (COT or τ_{cld}) and particle effective radius (CER or r_{cld} ,
420 unit= μm) (or cloud optical and microphysical properties) primarily characterizes the
421 radiative properties of clouds, highlighting their influence on the equilibrium of Earth's
422 radiation budget (Platnick et al., 2017). These two parameters are commonly used in
423 general circulation model (GCM) to define cloud parameterization schemes for climate
424 modeling (Chou et al., 1998). The cloud optical and microphysical properties algorithm
425 during the daytime (solar zenith angle $< 65^\circ$) utilizes the reflected solar radiation



426 measured by a non-absorbing channel (0.64 μm) to retrieve cloud optical thickness (τ_{cld}).
427 Additionally, it uses the reflected solar radiation measured by an absorbing channel
428 (2.23 μm) to retrieve cloud particle effective radius (r_{cld}) (Walther et al., 2011). The
429 fundamental physical principle of this algorithm is to leverage the sensitivities of the
430 non-absorbing and absorbing channels to cloud optical thickness (τ_{cld}) and cloud
431 particle effective radius (r_{cld}) in the atmospheric radiative transfer process, as
432 demonstrated by a previous study (Nakajima and King, 1990).

433 The water and ice cloud optical and radiative properties look-up tables (LUT) with
434 a modified Gamma size distribution for fast retrieval were built based on spherical
435 particle with the scattering properties given by the Mie theory and MODIS Collection-
436 6 severely roughened aggregated columns ice crystal (Baum et al., 2007; Min et al.,
437 2017a; Platnick et al., 2017), respectively. By utilizing the similar 1DVAR algorithm
438 discussed in Section 3.3, along with water/ice cloud LUTs, observed reflectance at 0.64
439 and 2.23 μm channels, and additional ancillary data, the optimal cloud optical thickness
440 (τ_{cld}) and cloud particle effective radius (r_{cld}) can be iteratively calculated using the OE
441 algorithm (Walther et al., 2011). Differing from Equation (2), the variables or first-
442 order partial derivative from forward cloud reflectance model in the Jacobi matrix are
443 derived from a formula for solar reflectance observed by satellite, which can be written
444 as follows (Nakajima and King, 1990):

$$445 R_{obs} = R_{cld} + \frac{A_s}{1 - A_s R'_{cld}} T_{cld} T'_{cld}, \quad (8)$$

446 where R_{obs} is the total cloud bidirectional reflectance function at the top of the
447 atmosphere (TOA). A_s is the albedo at the Lambertian surface of a uniform single-layer
448 cloud. R_{cld} and T_{cld} signify the cloud reflectance and downward transmittance (diffuse
449 and direct), respectively. R'_{cld} and T'_{cld} are the cloud spherical albedo and the
450 transmittance below the cloud, respectively. After retrieving τ_{cld} and r_{cld} , ice and liquid
451 cloud water paths (IWP/LWP) are calculated using empirical formulas (Bennartz, 2007;
452 Heymsfield et al., 2007), which are expressed as follows:

$$453 LWP = \frac{5}{9} \tau_{cld} r_{cld} \rho, \quad (9)$$

$$454 IWP = \frac{\tau_{cld}^{1/0.84}}{0.065}, \quad (10)$$

455 where ρ is the density of liquid water (=1.0 g/cm^3).

456 Figure 6 shows the cloud optical depth and effective radius comparisons between
457 the H9/AHI GEO satellite and MODIS (Platnick et al., 2017) at 05:40 UTC on October



458 30, 2023. We find the consistent retrieval results between these two different COT and
459 CER products. Besides, Figures 6e and 6f respectively show the comparisons of the
460 four months COT and CER from MODIS and H9/AHI data over the SCS with the
461 related scores, such as MAE, MBE, R and RMSE. The differences are likely to be
462 attributed to the different spatial resolutions and retrieval algorithms used between
463 these two satellite products (Letu et al., 2019; Wang et al., 2024).

464

465 3.5 Layered precipitable water and atmospheric instability indices

466 The atmospheric temperature and humidity profiles provide valuable information
467 about the vertical distribution of water vapor and temperature at various altitudes. This
468 is very crucial for studying cloud formation, precipitation patterns, and the intricate
469 processes of the water cycle, and accurate numerical weather forecasting and climate
470 modeling (Charlesworth et al., 2023; Li et al., 2016; Zheng et al., 2015; Zhu et al.,
471 2023). In this investigation, the layered precipitable water (LPW) product obtained
472 from H8/9-AHI only provides clear sky (refer to the flowchart in Figure 1) temperature
473 and humidity profiles and atmospheric instability indices. The next few satellite
474 products in Sections 3.6 and 3.7 will also be processed only in clear sky pixels. The
475 temperature and humidity profiles will be integrated into three distinct layers for the
476 output satellite product (High layer: from 700 to 300 hPa; Middle layer: from 900 to
477 700 hPa; Low layer: from the surface to 900 hPa).

478 This physics-based LPW retrieval algorithm uses the BT observations at 6.2, 6.9,
479 7.3, 8.5, 10.4, 11.2, 12.3, and 13.3 μm channels to retrieve temperature and humidity
480 profiles. Since the temperature and humidity profiles can only be retrieved from clear-
481 sky pixels, we can express the forward IR radiative transfer equation observed by
482 satellite sensor as follows (Li et al., 2012; Li et al., 2000):

$$483 I_{obs}(\lambda) = \varepsilon_s(\lambda)B_s(\lambda)T_s(\lambda) - \int_0^{p_s} B(\lambda)dT(0, p) + [1 - \varepsilon_s(\lambda)] \int_0^{p_s} B(\lambda)dT'(\lambda), \quad (11)$$

484 where T is the atmospheric transmittance above the pressure p . Subscript s signifies the
485 surface, $T' = T_s^2/T$. Similar to the OE method mentioned above, the cost function for
486 retrieving temperature and humidity profiles can be written as follows:

$$487 \zeta = [x - x_a]^T \gamma Cov_a^{-1} [x - x_a] + [y - M(x)]^T Cov_y^{-1} [y - M(x)], \quad (12)$$

488 where the new added variable γ is the regularization parameter (or smoothing factor)
489 compared to Eq. (5). The introduction of the parameter γ aims to achieve faster
490 convergence and improve solution stability. The iterative 1DVAR algorithm can



491 increase or decrease parameter γ by determining the first-order variation of Eq. (11) (Li
492 et al., 2000). The first guessed temperature and humidity profiles for iterative retrieval
493 are obtained from spatial-temporally matched GFS-NWP data.

494 After retrieving the optimal temperature and humidity profiles, it will calculate
495 five atmospheric instability indices, including LI (Lifted Index), CAPE (Convective
496 Available Potential Energy), TT (Total Totals), KI (K Index), and SI (Showalter Index).
497 In weather forecasting, these indices can characterize the degree of development of
498 atmospheric instability features and provide the forecaster with a general idea of the
499 convective forcing. For instance, the LI represents the level of atmospheric
500 thermodynamic instability. A positive LI value indicates stability ($0 < LI$), while a
501 negative LI value suggests varying degrees of instability ($-3 < LI < 0$ marginally unstable,
502 $-6 < LI < -3$ moderately unstable, $-9 < LI < -6$ very unstable, and $LI < -9$ extremely unstable).
503 The valid ranges and usages of these five atmospheric instability indices could refer to
504 Table 1 and the study from Li et al., 2012. Note that, considering the specific retrieval
505 efficiency (processing LPW over the SCS region takes approximately 20~25 minutes)
506 of the H8/9-AHI LPW product, we have set the retrieval frequency for LPW to 30
507 minutes.

508 Figure 7 presents a comparison between the LPW, encompassing total
509 precipitable water and water vapors at low, middle, and high layers, derived from the
510 H9/AHI GEO satellite and ERA5 reanalysis data at 09:00 UTC on January 4, 2023,
511 specifically over the SCS. The right column panel displays associated H9/AHI CAPE,
512 K, LI, and Showalter indices. Except for the water vapors at the high layer (700-
513 300hPa), the remaining LWP products exhibit negligible differences compared to the
514 ERA5 reanalysis data in Figure 7.

515 To further validate the LPW products derived from H9/AHI, we conducted
516 comparisons against ERA5 reanalysis data for LPWs over a four-month period
517 mentioned above (January, April, July, and October of 2023). Figure 8 depicts the
518 comparison results for total precipitable water and LPWs at three distinct layers. The
519 correlation coefficients (R) for the LPWs at low, middle, and high layers, along with
520 total precipitable water, are respectively 0.917, 0.849, 0.831, and 0.869. These high
521 correlation coefficients indicate the relatively high quality of this product from the
522 NANO_SCS system.

523

524 *3.6 Land and sea surface temperatures*



525 Land and sea surface temperatures (LST and SST) are essential variables
526 frequently utilized in climate research community (Cai et al., 2022; Hong et al., 2022).
527 In this study, we incorporated a classical land surface temperature algorithm (Ulivieri
528 and Cannizzaro, 1985) into the NANO_SCS system, using split-windows channels of
529 H8/9-AHI (11.2 and 12.3 μm). This modified algorithm was also implemented as the
530 operational LST algorithm for the FY-4A GEO satellite (Dong et al., 2023) in China
531 Meteorological Administration (CMA), which can be easily expressed as follows:

$$532 \quad LST = C + A_1 BT_{11\mu\text{m}} + A_2 (BT_{11\mu\text{m}} - BT_{12\mu\text{m}}) + A_3 \varepsilon_s + D (BT_{11\mu\text{m}} -$$
$$533 \quad BT_{12\mu\text{m}}) (\sec\theta - 1), \quad (13)$$

534 where C , A_{1-3} , and D are the fitting coefficients, respectively. θ represents the satellite
535 zenith angle. ε_s is the surface emissivity. To account for the uncertainties in the LST
536 algorithm caused by water vapor, we conducted regression analysis using MODTRAN
537 V4.2 (Berk et al., 2000; Dong et al., 2023; Min et al., 2022) to derive fitting coefficients
538 for four distinct groups: daytime dry, daytime moist, nighttime dry, and nighttime moist
539 conditions. A threshold of water vapor content = 2.0 g/cm^2 was utilized to classify the
540 atmosphere as either dry or moist. This threshold value was obtained from matched
541 GFS-NWP data.

542 The classical and simplified Non-Linear Sea Surface Temperature (NLSST)
543 algorithm was used here to retrieve SST of H8/9-AHI (Walton et al., 1998), which is
544 expressed as follows:

$$545 \quad SST = a_0 + a_1 BT_{11\mu\text{m}} + a_2 (BT_{11\mu\text{m}} - BT_{12\mu\text{m}}) + a_3 (BT_{11\mu\text{m}} -$$
$$546 \quad BT_{12\mu\text{m}}) (\sec\theta - 1), \quad (14)$$

547 where a_{0-3} are the fitting coefficients. The NOAA latest OISST (optimum interpolation
548 sea surface temperature) are used here to obtain fitting coefficients in Eq. (14) (Huang
549 et al., 2021; Reynolds et al., 2007). This global SST dataset, with a $0.25^\circ \times 0.25^\circ$
550 horizontal resolution, covers the period from 1981 to the present.

551 Figure 9 shows the LST and SST comparisons between H9/AHI GEO satellite and
552 MODIS at 18:40 UTC on October 29, 2023. From this figure, we find the consistent
553 results of LST and SST between our results and MODIS official products. Figures 9e
554 and 9f also shows the comparisons of the four months LST and SST from MODIS and
555 H9/AHI data over the SCS. The correlation coefficients (R) of these two products are
556 about 0.97.

557



558 3.7 Vegetation and water indices

559 Vegetation and water indices, such as NDVI (Normalized Difference Vegetation
560 Index), NDSI (Normalized Differential Snow Index), NDWI (Normalized Differential
561 Water Index), and LSWI (Land Surface Water Index), are commonly utilized for
562 climate change, vegetation growth, urbanization, flood monitoring, etc. (Zheng et al.,
563 2021). In the NANO_SCS system, these indices are calculated for clear-sky pixels
564 during daytime using H8/9-AHI and are expressed as follows:

$$565 \quad NDVI = (Ref_{0.86\mu m} - Ref_{0.64\mu m}) / (Ref_{0.86\mu m} + Ref_{0.64\mu m}), \quad (15)$$

$$566 \quad NDSI = (Ref_{1.6\mu m} - Ref_{0.64\mu m}) / (Ref_{1.6\mu m} + Ref_{0.64\mu m}), \quad (16)$$

$$567 \quad NDWI = (Ref_{0.64\mu m} - Ref_{2.23\mu m}) / (Ref_{0.64\mu m} + Ref_{2.23\mu m}), \quad (17)$$

$$568 \quad LSWI = (Ref_{0.86\mu m} - Ref_{1.6\mu m}) / (Ref_{0.86\mu m} + Ref_{1.6\mu m}), \quad (18)$$

569 where *Ref* represents the reflectance observed by satellite visible and near infrared
570 bands during the daytime. Unfortunately, in this study, the lack of a 0.47 μ m channel
571 prevents the computation of the Enhanced Vegetation Index (EVI). Figure 10 shows
572 the clear-sky NDVI, NDSI, NDWI, and LSWI maps from H9/AHI at 04:00 UTC on
573 December 1, 2023 over the SCS, which were generated by the NANO_SCS system.

574

575 4. Data availability

576 The Japanese Himawari-8/9 (H8/9) geostationary (GEO) satellites are
577 strategically positioned over the South China Sea (SCS), spanning from November 3,
578 2022, to the present. It mainly providing cloud mask, fraction, height, phase, optical
579 and microphysical properties, layered precipitable water, and sea surface temperature
580 products, within a temporal resolution of 10 minutes and a gridded resolution of 0.05°
581 \times 0.05°. Users can freely access sample HDF-formatted files and data download
582 instruction in PDF format of the South China Sea datasets at
583 <https://doi.org/10.6084/m9.figshare.25015853> (Liu, 2024). Besides, to access related
584 NRT satellite products, a quick-view website, data download FTP (File Transfer
585 Protocol), and user account information (password) are respectively the URLs:
586 [<http://meteorsatellite.hellosea.org.cn/#/index>], <ftp://www.hellosea.org.cn>, and
587 [smlweix \(sml#456@\)](mailto:smlweix@sml#456@).

588

589 5. Summary

590 This investigation provides a comprehensive introduction to the key GEO satellite
591 science products generated by the NANO_system and their evaluation. It offers near-



592 real-time atmospheric and oceanic science products of Himawari-8/9 geostationary
593 satellites over the South China Sea from November 13, 2022, to the present. Positioned
594 at 140.7°E and 0° longitude, the H8/9 geostationary satellites mainly cover East Asia,
595 Oceania, and the Indian Ocean. The standard NRT Level-2 satellite science products
596 encompass the region between 0° to 40°N latitude and 100°E to 140°E longitude with
597 a grid resolution of 0.05° × 0.05° and a 10-minute interval (except for LPW products,
598 retrieved every 30 minutes). These products are derived from 14 spectral channels with
599 a 4km horizontal resolution.

600 The NANO_system provides a range of atmospheric and oceanic products,
601 including cloud mask, fraction, height, phase, optical and microphysical properties,
602 layered precipitable water, land surface temperature, sea surface temperature, and more.
603 These near-real-time satellite products were rigorously evaluated against independent
604 datasets, including MODIS satellite-based products and ERA5 reanalysis data. The
605 results highlight strong consistency between NRT H8/9 geostationary satellite
606 atmospheric and oceanic science products and the reference data from similar sensors
607 and ERA5 over the South China Sea.

608 Future continuation of atmospheric and oceanic science products generated by the
609 NANO_SCS system is also operated and secured by the Southern Marine Science and
610 Engineering Guangdong Laboratory (Zhuhai) in China. Preparations are underway for
611 new products such as atmospheric motion vectors (AMV) and quantitative precipitation
612 estimates (QPE) in near-real-time production. Besides, the qualities of current GEO
613 satellite products will be further validated and enhanced in the future. Chinese FY-4C
614 GEO satellite, scheduled for launch in 2025 or 2026, will offer higher spatial resolution
615 and additional channels, including an IR hyperspectral sounder, to further extend and
616 improve the NANO_SCS-system-based data records for atmospheric and oceanic
617 parameters.

618

619

620 **Author contributions.** JL and MM contributed to designing the research; MM, JL, and
621 WW implemented the research and wrote the original draft; JL supervised the research;
622 all co-authors revised the paper and contributed to the writing.

623

624 **Competing interests.** The contact author has declared that none of the authors has any
625 competing interests.



626

627 **Disclaimer.** Publisher's note: Copernicus Publications remains neutral with regard to
628 jurisdictional claims in published maps and institutional affiliations.

629

630 **Acknowledgments.** The authors would like to thank JMA, U.S. NASA MODIS group
631 and ECMWF for freely providing Himawari-8/9 (<ftp.ptree.jaxa.jp>), MODIS
632 (<https://search.earthdata.nasa.gov/search>), and ERA5 reanalysis
633 (<https://cds.climate.copernicus.eu/cdsapp#!/home>) data. The authors also would like to
634 thank NOAA for freely providing GFS-NWP
635 (<https://nomads.ncep.noaa.gov/pub/data/nccf/com/gfs/>) and OISST
636 ([https://www.ncei.noaa.gov/data/sea-surface-temperature-optimum-
637 interpolation/v2.1/access/avhrr/](https://www.ncei.noaa.gov/data/sea-surface-temperature-optimum-
637 interpolation/v2.1/access/avhrr/)) data, and the GOES-R AWG. Besides, we also thanks
638 Dr. Lixin Dong of China National Satellite Meteorological Center who freely provide
639 LST algorithm code. This study was supported by the Southern Marine Science and
640 Engineering Guangdong Laboratory (Zhuhai) (Grant SML2021SP102 and
641 SML2022SP401), National Natural Science Foundation of China under Grants
642 42175086, FengYun Meteorological Satellite Innovation Foundation under Grant FY-
643 APP-ZX-2022.0207, Innovation Group Project of Southern Marine Science and
644 Engineering Guangdong Laboratory (Zhuhai) (No. SML2023SP208). Finally, we
645 would also like to thank the editor and anonymous reviewers for their thoughtful
646 suggestions and comments.

647

648

649

650

651

652

653

654

655

656



657

658

659

660

661 **References**

- 662 Baum, B. A., P. Yang, S. Nasiri, A. J. Heidinger, A. Heymsfield, and J. Li: Bulk
663 scattering properties from the remote sensing of ice clouds. Part III: High
664 resolution spectral models from 100 to 3250 cm⁻¹, *Journal of Applied*
665 *Meteorology and Climatology*, *46*, 423 - 434, doi:10.1175/JAM2473.1, 2007.
- 666 Bennartz, R.: Global assessment of marine boundary layer cloud droplet number
667 concentration from satellite, *Journal of Geophysical Research - Atmospheres*,
668 *112*, D02201, doi:10.1029/2006JD007547, 2007.
- 669 Berk, A., G. P. Anderson, P. K. Acharya, J. H. Chetwynd, L. S. Bernstein, E. P. Shettle,
670 M. W. Matthew, and S. M. Adler-Golden (2000), MODTRAN4 user's manual,
671 edited, Air Force Research Laboratory.
- 672 Bessho, K., et al.: An introduction to Himawari-8/9—Japan's new-generation
673 geostationary meteorological satellites, *Journal of the Meteorological Society*
674 *of Japan*, *94*, 151-183, doi:10.2151/jmsj.2016-009, 2016.
- 675 Cai, W., B. Ng, G. Wang, A. Santoso, L. Wu, and K. Yang: Increased ENSO sea surface
676 temperature variability under four IPCC emission scenarios, *Nature Climate*
677 *Change*, *12*, 228–231, 2022.
- 678 Charlesworth, E., et al.: Stratospheric water vapor affecting atmospheric circulation,
679 *Nature Communications*, *14*, 3925, doi:10.1038/s41467-023-39559-2, 2023.
- 680 Chou, M.-D., M. J. Suarez, C.-H. Ho, M. M.-H. Yan, and K.-T. Lee: Parameterizations
681 for cloud overlapping and shortwave single-scattering properties for use in
682 general circulation and cloud ensemble models, *J Climate*, *11*, 202-214,
683 doi:10.1175/1520-0442(1998)011<0202:PFCOAS>2.0.CO;2, 1998.
- 684 Ding, Y., and Y. Liu: Onset and the evolution of the Summer Monsoon over the South
685 China Sea during SCSMEX Field Experiment in 1998, *Journal of the*
686 *Meteorological Society of Japan*, *V79*, 255-276, doi:10.2151/jmsj.79.255, 2001.
- 687 Dong, L., S. Tang, F. Wang, M. Cosh, X. Li, and M. Min: Inversion and validation of
688 FY-4A official land surface temperature product, *Remote Sensing*, *15*, 2437,
689 doi:10.3390/rs15092437 2023.
- 690 Heidinger, A., and M. Pavolonis: Gazing at cirrus clouds for 25 years through a split
691 window, part 1: Methodology, *Journal of Applied Meteorology and Climatology*,
692 *48*, 1110-1116, doi:10.1175/2008JAMC1882.1, 2009.
- 693 Heidinger, A. K., A. T. Evan, M. J. Foster, and A. Walther: A naive Bayesian cloud-
694 detection scheme derived from CALIPSO and applied within PATMOS-x,
695 *Journal of Applied Meteorology and Climatology*, *51*, 1129–1144,
696 doi:10.1175/JAMC-D-11-02.1, 2012.



- 697 Hersbach, H., et al.: The ERA5 global reanalysis, *Quarterly Journal of the Royal*
698 *Meteorological Society*, *146*, 1999–2049, doi:10.1002/qj.3803, 2020.
- 699 Heymsfield, A. J., S. Matrosov, and B. Baum: Ice water path-optical depth relationships
700 for cirrus and deep stratiform ice cloud layers, *J Appl Meteorol*, *42*, 1369–1390,
701 doi:10.1175/1520-0450(2003)042<1369:IWPDRF>2.0.CO;2, 2007.
- 702 Hong, F., W. Zhan, F.-M. Göttsche, Z. Liu, P. Dong, H. Fu, F. Huang, and X. Zhang: A
703 global dataset of spatiotemporally seamless daily mean land surface
704 temperatures: generation, validation, and analysis, *Earth System Science Data*,
705 *14*, 3091–3113, doi:10.5194/essd-14-3091-2022, 2022.
- 706 Huang, B., C. Liu, V. Banzon, E. Freeman, G. Graham, B. Hankins, T. Smith, and H.-
707 M. Zhang: Improvements of the Daily Optimum Interpolation Sea Surface
708 Temperature (DOISST) Version 2.1, *J Climate*, *34*, 2923–2939,
709 doi:10.1175/JCLI-D-20-0166.1, 2021.
- 710 Husi, L., T. M. Nagao, T. Y. Nakajima, J. Riedi, H. Ishimoto, A. J. Baran, H. Shang, M.
711 Sekiguchi, and M. Kikuchi: Ice cloud properties from Himawari-8/AHI next-
712 generation geostationary satellite: Capability of the AHI to monitor the DC
713 cloud generation process, *IEEE Transactions on Geoscience and Remote*
714 *Sensing*, *57*, 3229–3239, doi:10.1109/TGRS.2018.2882803, 2019.
- 715 Jiang, J., T. Zhou, Y. Qian, C. Li, F. Song, H. Li, X. Chen, W. Zhang, and Z. Chen:
716 Precipitation regime changes in High Mountain Asia driven by cleaner air,
717 *Nature*, doi:10.1038/s41586-023-06619-y, 2023.
- 718 Kim, D., M. Gu, T.-H. Oh, E.-K. Kim, and H.-J. Yang: Introduction of the advanced
719 meteorological imager of Geo-Kompsat-2a: In-orbit tests and performance
720 validation, *Remote Sensing*, *13*, 1303, doi:10.3390/rs13071303, 2021.
- 721 King, M. D., S. C. Tsay, S. E. Planick, M. Wang, and K. N. Liou: Cloud retrieval
722 algorithms: Optical thickness, effective particle radius, and thermodynamic
723 phase, *NASA MODIS Algorithm Theoretical Basis Documents*, 1997.
- 724 Koseki, S., K. Tieh-Yong, and T. Chee-Kiat: Effects of the cold tongue in the South
725 China Sea on the monsoon, diurnal cycle and rainfall in the Maritime Continent,
726 *Quarterly Journal of the Royal Meteorological Society*, *139*, 1566–1582,
727 doi:10.1002/qj.2052, 2013.
- 728 Lai, R., S. Teng, B. Yi, H. Letu, M. Min, S. Tang, and C. Liu: Comparison of cloud
729 properties from Himawari-8 and FengYun-4A geostationary satellite
730 radiometers with MODIS cloud retrievals, *Remote Sensing*, *11*, 1703,
731 doi:10.3390/rs11141703, 2019.
- 732 Letu, H., T. M. Nagao, T. Y. Nakajima, J. Riedi, H. Ishimoto, A. J. Baran, H. Shang, M.
733 Sekiguchi, and M. Kikuchi: Ice cloud properties from Himawari-8/AHI next-
734 generation geostationary satellite: Capability of the AHI to monitor the DC
735 cloud generation process, *IEEE Transactions on Geoscience and Remote*
736 *Sensing*, *57*, 3229–3239, doi:10.1109/tgrs.2018.2882803, 2019.
- 737 Letu, H., et al.: High-resolution retrieval of cloud microphysical properties and surface
738 solar radiation using Himawari-8/AHI next-generation geostationary satellite,
739 *Remote Sensing of Environment*, *239*, 111583, doi:10.1016/j.rse.2019.111583,



- 740 2020.
- 741 Levenberg, K.: A method for the solution of certain non-linear problems in least squares,
742 *Quarterly of Applied Mathematics*, *2*, 164-168, 1944.
- 743 Li, J., W. P. Menzel, T. J. Schmit, and J. Schmetz: Applications of geostationary
744 hyperspectral infrared sounder observations – progress, challenges, and future
745 perspectives, *Bulletin of the American Meteorological Society*,
746 doi:10.1175/BAMS-D-21-0328.1, 2022a.
- 747 Li, J., T. J. Schmit, X. Jin, and G. Martin: GOES-R Advanced Baseline Imager (ABI)
748 Algorithm Theoretical Basis Document For Legacy Atmospheric Moisture
749 Profile, Legacy Atmospheric Temperature Profile, Total Precipitable Water, and
750 Derived Atmospheric Stability Indices NOAA Goes-R ATBD, 109, 2012.
- 751 Li, J., P. Wang, H. Han, J. Li, and J. Zheng: On the assimilation of satellite sounder data
752 in cloudy skies in numerical weather prediction models, *Journal of*
753 *Meteorological Research*, *30*, 169–182, 2016.
- 754 Li, J., W. W. Wolf, W. P. Menzel, W. Zhang, H.-L. Huang, and T. H. Achtor: Global
755 soundings of the atmosphere from ATOVS measurements: The algorithm and
756 validation, *Journal of Applied Meteorology*, *39*, 1248–1268,
757 doi:10.1175/1520-0450(2000)039<1248:GSOTAF>2.0.CO;2, 2000.
- 758 Li, Y., G. Ren, Q. Wang, L. Mu, and Q. Niu: Marine heatwaves in the South China Sea:
759 Tempo-spatial pattern and its association with large-scale circulation, *Remote*
760 *Sensing*, *14*, 5829, doi:10.3390/rs14225829, 2022b.
- 761 Liang, Y., M. Min, Y. Yu, X. Wang, and P. Xia: Assessing diurnal cycle of cloud covers
762 of Fengyun-4A geostationary satellite based on the manual observation data in
763 China, *IEEE Transactions on Geoscience and Remote Sensing*, *61*,
764 doi:10.1109/TGRS.2023.3256365, 2023.
- 765 Liu, B., Y. Liu, G. Wu, J. Yan, J. He, and S. Ren: Asian summer monsoon onset barrier
766 and its formation mechanism, *Climate Dynamics*, *45*, 711–726,
767 doi:10.1007/s00382-014-2296-0, 2014.
- 768 Liu Jian, Y. J., Lin Chuyong, He Min, Liu Haiyan, Min Min, Wang Wei (2024), Near
769 real-time atmospheric and oceanic science products of Himawari-8/9
770 geostationary satellites over the South China Sea, edited, figshare. Dataset.,
771 doi:<https://doi.org/10.6084/m9.figshare.25015853>.
- 772 Ma, Z., J. Li, W. Han, Z. Li, Q. Zeng, W. P. Menzel, T. J. Schmit, D. Di, and C.-Y. Liu:
773 Four - dimensional wind fields from geostationary hyperspectral infrared
774 sounder radiance measurements with high temporal resolution, *Geophys Res*
775 *Lett*, *48*, e2021GL093794, doi:10.1029/2021GL093794, 2021.
- 776 Martin, D. W., and M. R. Howland: Rainfall over the Arabian Sea during the onset of
777 the 1979 monsoon, *Nature*, *300*, 628–630, 1982.
- 778 Min, M., et al.: Estimating summertime precipitation from Himawari-8 and global
779 forecast system based on machine learning, *IEEE Transactions on Geoscience*
780 *and Remote Sensing*, *57*, 2557-2570, doi:10.1109/TGRS.2018.2874950, 2019.
- 781 Min, M., B. Chen, N. Xu, X. He, X. Wei, and M. Wang: Nonnegligible diurnal and
782 long-term variation characteristics of the calibration biases in Fengyun-



- 783 4A/AGRI infrared channels based on the oceanic drifter data, IEEE
784 Transactions on Geoscience and Remote Sensing, *60*, 1-15,
785 doi:10.1109/TGRS.2022.3160450, 2022.
- 786 Min, M., J. Deng, C. Liu, N. Lu, X. Hu, L. Chen, J. Guo, P. Zhang, Q. Lu, and L. Wang:
787 An investigation of the implications of lunar illumination spectral changes for
788 Day/Night Band based cloud property retrieval due to lunar phase transition,
789 Journal of Geophysical Research: Atmospheres, *122*, 9233-9244,
790 doi:10.1002/2017JD027117, 2017a.
- 791 Min, M., J. Li, F. Wang, Z. Liu, and W. P. Menzel: Retrieval of cloud top properties
792 from advanced geostationary satellite imager measurements based on machine
793 learning algorithms, Remote Sensing of Environment, *239*, 111616,
794 doi:10.1016/j.rse.2019.111616 2020.
- 795 Min, M., et al.: Developing the science product algorithm testbed for Chinese next-
796 generation geostationary meteorological satellites: Fengyun-4 series, Journal of
797 Meteorological Research, *31*, 708-719, doi:10.1007/s13351-017-6161-z, 2017b.
- 798 Mülmenstädt, J., M. Salzmann, J. E. Kay, M. D. Zelinka, P.-L. Ma, C. Nam, J.
799 Kretzschmar, S. Hörmig, and J. Quaas: An underestimated negative cloud
800 feedback from cloud lifetime changes, Nature Climate Change, *11*, 508-513,
801 doi:10.1038/s41558-021-01038-1, 2021.
- 802 Nakajima, T., and M. D. King: Determination of the optical thickness and effective
803 particle radius of clouds from reflected solar radiation measurements. Part I:
804 Theory, J Atmos Sci, *48*, 728-750, 1990.
- 805 Niu, Q., and Y. Feng: Relationships between the typhoon-induced wind and waves in
806 the northern South China Sea, Geophys Res Lett, *48*, e2020GL091665,
807 doi:10.1029/2020GL091665, 2021.
- 808 Noh, Y.-J., J. M. Forsythe, S. D. Miller, C. J. Seaman, Y. Li, A. K. Heidinger, D. T.
809 Lindsey, M. A. Rogers, and P. T. Partain: Cloud-base height estimation from
810 VIIRS. Part II: A statistical algorithm based on A-Train satellite data, Journal of
811 Atmospheric and Oceanic Technology, *34*, 585-598, doi:10.1175/JTECH-D-
812 16-0110.1, 2017.
- 813 Parol, F., J. C. Buriez, G. Brogniez, and Y. Fouquart: Information content of AVHRR
814 channels 4 and 5 with respect to the effective radius of cirrus cloud particles, J
815 Appl Meteorol, *30*, 973-984, 1991.
- 816 Pavolonis, M.: GOES-R Advanced Baseline Imager (ABI) Algorithm Theoretical Basis
817 Document For Cloud Type and Cloud Phase Version 2.0, NOAA GOES-R
818 ATBD, 1-96, 2010a.
- 819 Pavolonis, M. J.: Advances in extracting cloud composition information from
820 spaceborne infrared radiances-A robust alternative to brightness temperatures.
821 Part I: Theory, Journal of Applied Meteorological Climatology, *49*, 1992-2012,
822 2010b.
- 823 Pavolonis, M. J., A. K. Heidinger, and T. Uttal: Daytime global cloud typing from
824 AVHRR and VIIRS: Algorithm description, validation, and comparisons J Appl
825 Meteorol, *44*, 804-826, 2005.



- 826 Platnick, S., M. D. King, S. A. Ackerman, W. P. Menzel, B. A. Baum, J. C. Riédi, and
827 R. A. Frey: The MODIS cloud products: Algorithms and examples from Terra,
828 IEEE Transactions on Geoscience and Remote Sensing, *41*, 459-473,
829 doi:10.1109/TGRS.2002.808301, 2003.
- 830 Platnick, S., et al.: The MODIS cloud optical and microphysical products: Collection 6
831 updates and examples from Terra and Aqua, IEEE Transactions On Geoscience
832 and Remote Sensing, *55*, 502-525, doi:10.1109/TGRS.2016.2610522, 2017.
- 833 Reynolds, R., T. M. Smith, C. Liu, D. Chelton, K. Casey, and M. Schlax: Daily high-
834 resolution-blended analyses for sea surface temperature, J Climate, *20*, 5473-
835 5496, doi:10.1175/2007JCLI1824.1, 2007.
- 836 Rodgers, C. D.: Inverse methods for atmospheric sounding: Theory and practice, 2000.
- 837 Schmit, T. J., P. Griffith, M. M. Gunshor, J. M. Daniels, S. J. Goodman, and W. J. Lehair:
838 A closer look at the ABI on the GOES-R Series Bulletin of the American
839 Meteorological Society, *98*, 681-698 doi:10.1175/BAMS-D-15-00230.1, 2017.
- 840 Soldi, G., et al.: Space-based global maritime surveillance. Part I: Satellite technologies,
841 IEEE Aerospace and Electronic Systems Magazine *36*, 8-28,
842 doi:10.1109/MAES.2021.3070862, 2021.
- 843 Ulivieri, C., and G. Cannizzaro: Land surface temperature retrievals from satellite
844 measurements, Acta Astronaut, *12*, 985-997, doi:10.1016/0094-
845 5765(85)90026-8, 1985.
- 846 Viúdez-Mora, A., C.-S. M., J. Calbó, and J. A. González: Modeling atmospheric
847 longwave radiation at the surface during overcast skies: The role of cloud base
848 height, Journal of Geophysical Research: Atmospheres, *120*, 199-214,
849 doi:10.1002/2014JD022310, 2015.
- 850 Walther, A., W. Straka, and A. K. Heidinger: GOES-R Advanced Baseline Imager (ABI)
851 algorithm theoretical basis document for daytime cloud optical and
852 microphysical properties (DCOMP), NOAA Goes-R ATBD, 2011.
- 853 Walton, C. C., W. G. Pichel, J. F. Sapper, and D. A. May: The development and
854 operational application of nonlinear algorithms for the measurement of sea
855 surface temperatures with the NOAA polar-orbiting environmental satellites,
856 Journal of Geophysical Research, *103*, 27999-28012, doi:10.1029/98JC02370,
857 1998.
- 858 Wang, B., F. Huang, Z. Wu, J. Yang, X. Fu, and K. Kikuchi: Multi-scale climate
859 variability of the South China Sea monsoon: A review, Dynamics of
860 Atmospheres and Oceans, *47*, 15-37, doi:10.1016/j.dynatmoce.2008.09.004,
861 2009.
- 862 Wang, F., M. Min, N. Xu, C. Liu, Z. Wang, and L. Zhu: Effects of linear calibration
863 errors at low temperature end of thermal infrared band: Lesson from failures in
864 cloud top property retrieval of FengYun-4A geostationary satellite, IEEE
865 Transactions on Geoscience and Remote Sensing, *60*, 5001511,
866 doi:10.1109/TGRS.2022.3140348, 2022.
- 867 Wang, G., S.-P. Xie, T. Qu, and R. X. Huang: Deep South China Sea circulation,
868 Geophys Res Lett, *38*, L05601, doi:10.1029/2010GL046626, 2011.



- 869 Wang, M., M. Min, J. Li, B. Chen, H. Lin, Z. Yao, N. Xu, and M. Zhang: Applicability
870 of physics-based and machine-learning-based algorithms of geostationary
871 satellite in retrieving the diurnal cycle of cloud base height, *Atmospheric
872 Chemistry and Physics Discussion*, 2024.
- 873 Wang, X., Q.-Y. Liu, D. Sui, and D. Wang: The imprint of the ENSO activities on the
874 South China Sea wave climate, *Ocean Dynamics*, *70*, 1315–1323,
875 doi:10.1007/s10236-020-01400-5, 2020.
- 876 Wang, X., M. Min, F. Wang, J. Guo, B. Li, and S. Tang: Intercomparisons of cloud mask
877 product among Fengyun-4A, Himawari-8 and MODIS, *IEEE Transactions on
878 Geoscience and Remote Sensing*, *57*, 8827–8839,
879 doi:10.1109/TGRS.2019.2923247 2019.
- 880 Whitaker, J. S., T. M. Hamill, X. Wei, Y. Song, and Z. Toth: Ensemble data assimilation
881 with the NCEP global forecast system, *Monthly Weather Review*, *136*, 463–482,
882 doi:10.1175/2007MWR2018.1, 2008.
- 883 Xia, P., M. Min, Y. Yu, Y. Wang, and L. Zhang: Developing a near real-time cloud cover
884 retrieval algorithm using geostationary satellite observations for photovoltaic
885 plants, *Remote Sensing*, *15*, 1141, doi:10.3390/rs15041141, 2023.
- 886 Xia, P., L. Zhang, M. Min, J. Li, Y. Wang, Y. Yu, and S. Jia: Accurate nowcasting on
887 cloud cover at solar photovoltaic plants using geostationary satellite images,
888 *Nature Communications*, *15*, 1–10, doi:10.1038/s41467-023-44666-1, 2024.
- 889 Xu, W., S. A. Rutledge, and K. Chudler: Diurnal cycle of coastal convection in the
890 South China Sea region and modulation by the BSISO34, 4297–4314,
891 doi:10.1175/JCLI-D-20-0308.1, 2021.
- 892 Yang, J., Z. Zhang, C. Wei, F. Lu, and Q. Guo: Introducing the new generation of
893 Chinese geostationary weather satellites, FengYun-4, *Bulletin of the American
894 Meteorological Society*, *98*, 1637–1658, doi:10.1175/BAMS-D-16-0065.1,
895 2017.
- 896 Zhao, G., and L. D. Girolamo: Cloud fraction errors for trade wind cumuli from EOS-
897 Terra instruments, *Geophys Res Lett*, *33*, L20802, doi:10.1029/2006GL027088,
898 2006.
- 899 Zheng, J., J. Li, T. J. Schmit, J. Li, and Z. Liu: The impact of AIRS atmospheric
900 temperature and moisture profiles on hurricane forecasts: Ike (2008) and Irene
901 (2011), *Advances in Atmospheric Sciences*, *32*, 319–335, 2015.
- 902 Zheng, Y., L. Tang, and H. Wang: An improved approach for monitoring urban built-up
903 areas by combining NPP-VIIRS nighttime light, NDVI, NDWI, and NDBI,
904 *Journal of Cleaner Production*, *328*, 129488, doi:10.1016/j.jclepro.2021.129488,
905 2021.
- 906 Zhou, R., X. Pan, Z. Xiaohu, X. Na, and M. Min: Research progress and prospects of
907 atmospheric motion vector based on meteorological satellite images, *Reviews of
908 Geophysics and Planetary Physics (In Chinese)*, *55*, 184–194,
909 doi:10.19975/j.dqyxx.2022-077, 2024.
- 910 Zhu, L., R. Zhou, D. Di, W. Bai, and Z. Liu: Retrieval of atmospheric water vapor
911 content in the environment from AHI/H8 using both physical and random forest



912 methods—A case study for typhoon Maria (201808), *Remote Sensing*, *15*, 498,
913 doi:10.3390/rs15020498, 2023.

914
915

916

917

918

919

920

921

922

923

924

925

926

927

928

929

930

931

932

933

934

935

936

937



938 **Tables and Figures**

939 **Table 1.** Primary NRT H8/9 GEO satellite atmospheric and oceanic science products
 940 and related variables generated by the NANO_SCS system.

Product Name (Abbr.)	Variable Name	Valid Value	Unit	Note
Cloud Mask (CLM)	Cloud_Mask	0=Cloudy; 1=Probably cloudy; 2=Probably clear; 3=Clear	None	
Cloud Fraction (CLF)	Cloud_Fraction	0-100	%	down-sampled 5×5 pixel box
Cloud Type and Phase (CLP)	Cloud_Type	0=Clear; 1=Spare; 2=Liquid water; 3=Supercooled water; 4=Mixed; 5=Optically thick ice; 6=Optically thin ice; 7=Multilayered ice; 8=Uncertainty	None	
	Cloud_Phase	0=Clear; 1=Liquid water; 2=Supercooled water; 3=Mixed; 4=Ice; 5=Uncertainty	None	
Cloud Top Properties (CTP)	Cloud_Top_Height	0-30000	m	
	Cloud_Top_Pressure	0-2000	hPa	
	Cloud_Top_Temperature	0-400	K	
	Cloud_Emissivity_at_11µm	0-100	%	
Cloud Optical and Microphysical Properties (COT)	Cloud_Optical_Depth	0-150	None	only daytime
	Cloud_Effective_Radius	0-100	µm	only daytime
	Cloud_Liquid_Water_Path	0-1000	g/m ²	only daytime
	Cloud_Ice_Water_Path	0-1000	g/m ²	only daytime
Cloud Base Properties (CBP)	Cloud_Base_Height	0-30000	m	only daytime
	Cloud_Base_Pressure	0-2000	hPa	only daytime
Sea Surface Temperature (SST)	Sea_Surface_Temperature	0-400	K	
Land Surface Temperature (LST)	Land_Surface_Temperature	0-400	K	
Vegetation/Water Indices (NDI)	NDVI (Normalized Difference Vegetation Index)	0-1.0	None	only daytime
	NDSI (Normalized Differential Snow Index)	0-1.0	None	only daytime
	NDWI (Normalized Differential Water Index)	0-1.0	None	only daytime
	LSWI (Land Surface Water Index)	0-1.0	None	only daytime
Layered Precipitable Water (LPW)	Total Precipitable Water	0-1000	mm	
	Water Vapor High	0-1000	mm	700-300hPa
	Water Vapor Middle	0-1000	mm	900-700hPa
	Water Vapor Low	0-1000	mm	Surface-900hPa
	CAPE_Index (Convective Available Potential Energy)	0-10000	J/kg	
	K_Index	-100-100	K	
	LI_Index (Lifted)	-100-100	°C	
	Showalter_Index	-100-100	°C	
TT_Index (Total totals)	-100-100	°C		

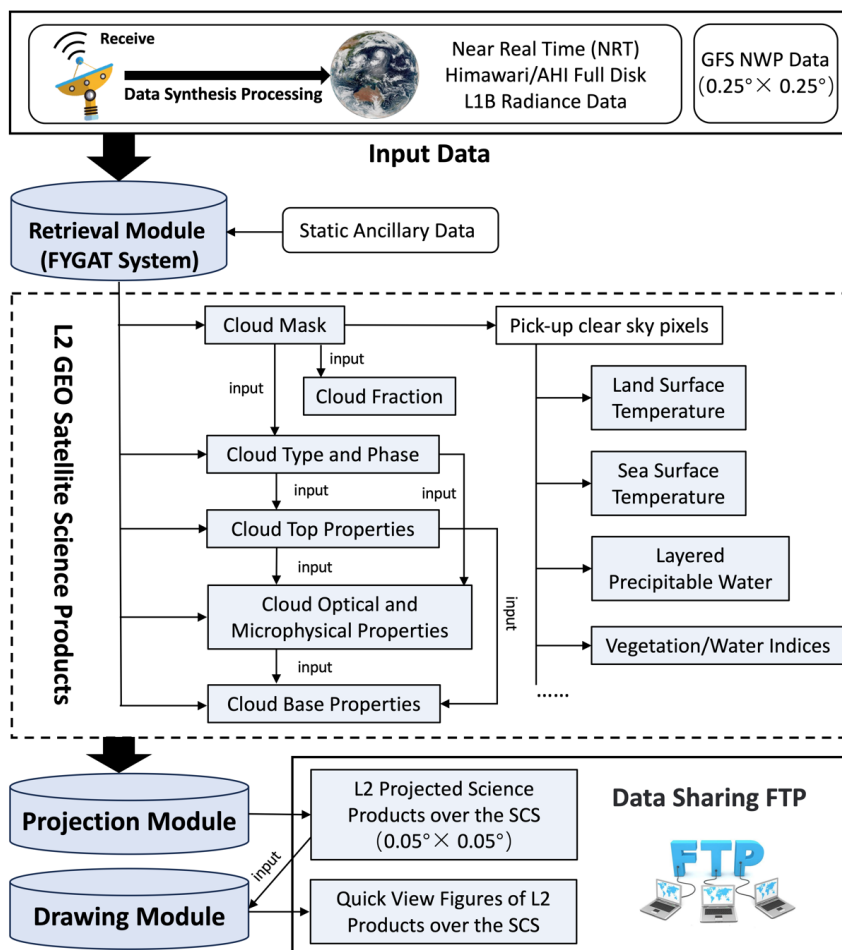
941

942

943



944



945

946 **Figure 1.** Flowchart of the NANO_SCS system. Dark gray shading represents key
 947 processing module; light gray shading represents satellite science product.

948

949

950

951

952

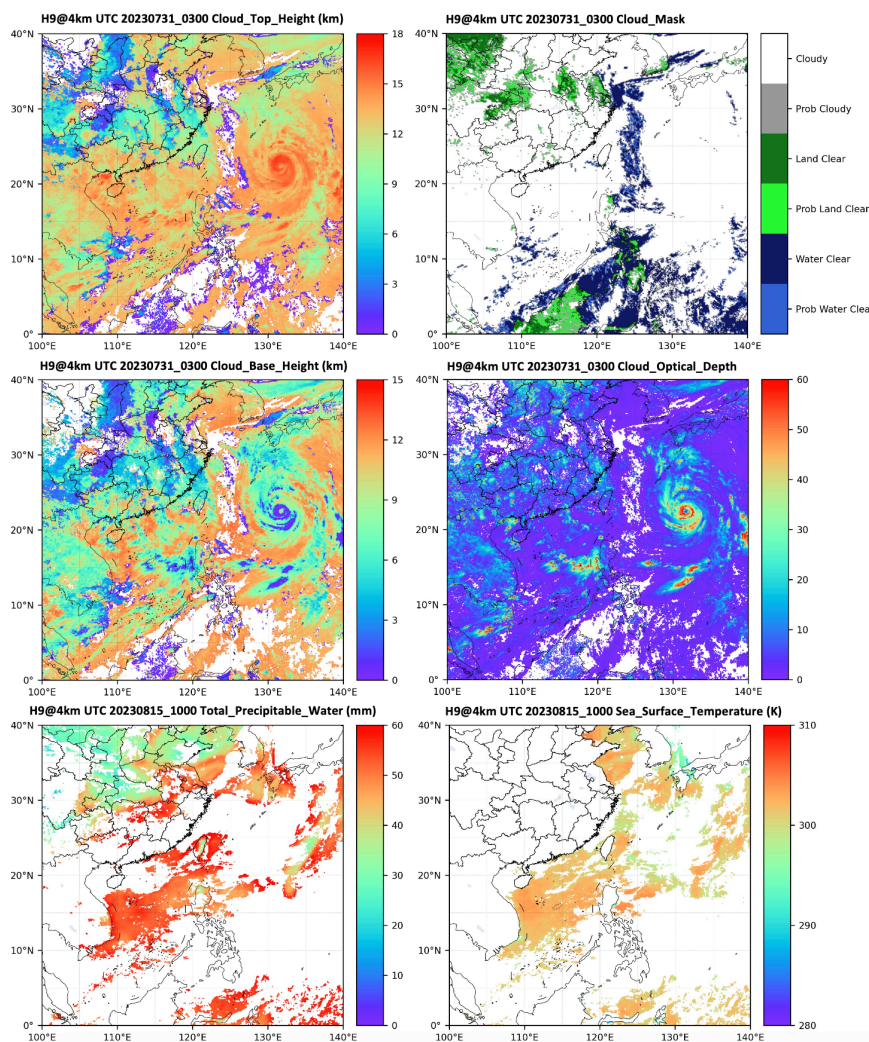
953

954

955



956



957

958 **Figure 2.** H9/AHI GEO satellite cloud top height (left top panel), cloud mask (right top
959 panel), cloud base height (left middle panel), cloud optical depth (right middle panel)
960 at 03:00 UTC on July 31, 2023, and atmospheric total precipitable water (left bottom
961 panel) and sea surface temperature (right bottom panel) at 10:00 UTC on August 15,
962 2023 over the SCS.

963

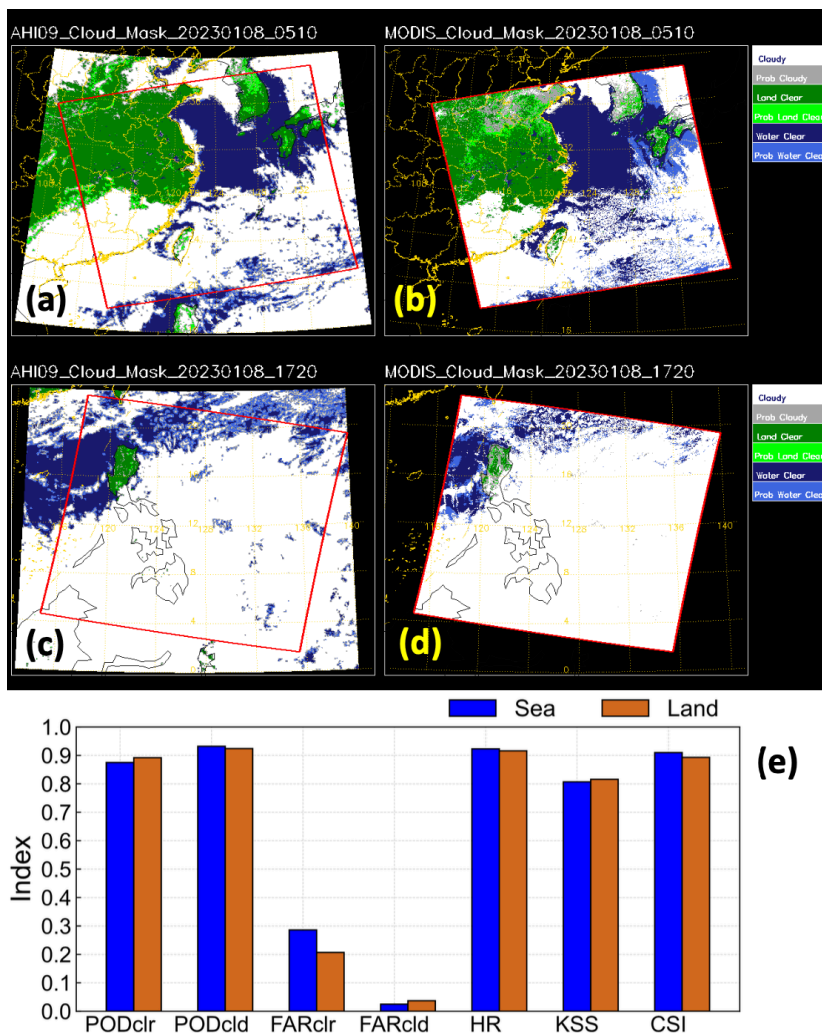
964

965

966



967

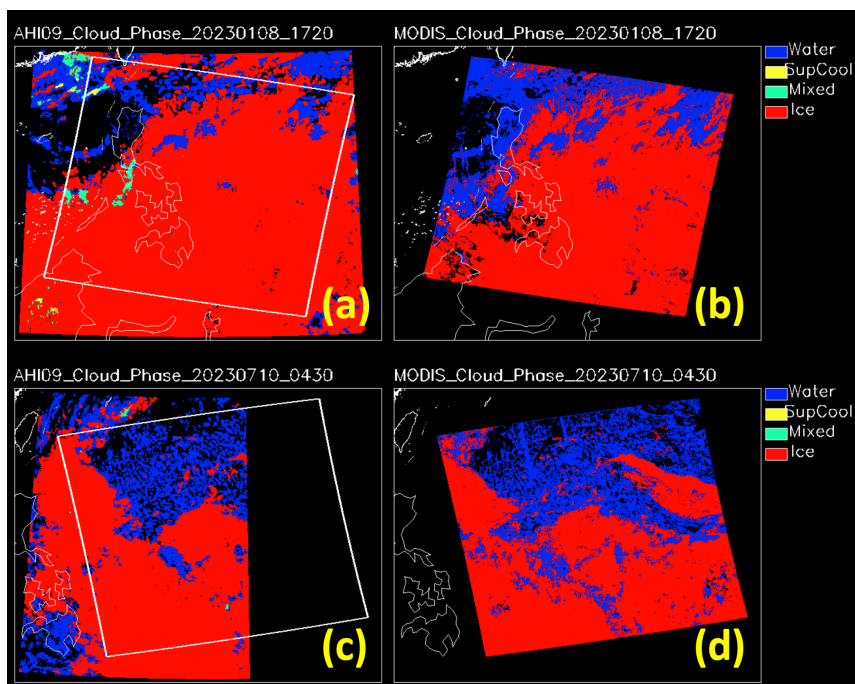


968
 969 **Figure 3.** Cloud mask comparisons between (a, c) H9/AHI GEO satellite and (b, d)
 970 MODIS at 05:10 (top panel) and 17:20 (middle panel) UTC on January 8, 2023. (e)
 971 POD, FAR, HR, and KSS scores of H9/AHI results for all the matched pixels over land
 972 (earthy yellow) and sea (blue) in January, April, July, and October of 2023. "clr" and
 973 "cld" respectively signify the clear and cloudy pixels.

974
 975
 976
 977

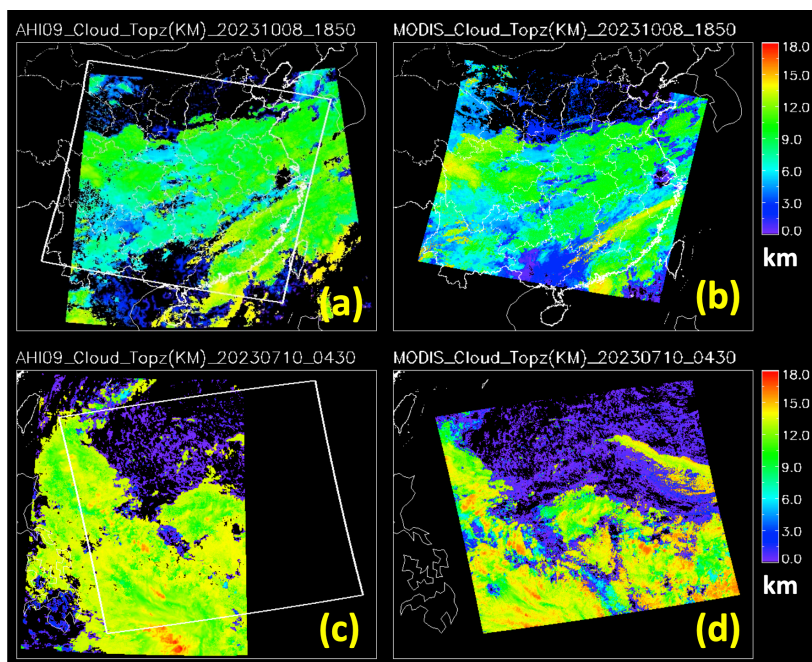


978
979
980



981
982 **Figure 4.** Cloud phase comparisons between (a, c) H9/AHI GEO satellite and (b, d)
983 MODIS at 05:10 UTC (top panel) on January 8, 2023 and 04:30 UTC (bottom panel)
984 on July 10, 2023.

985
986
987
988
989
990

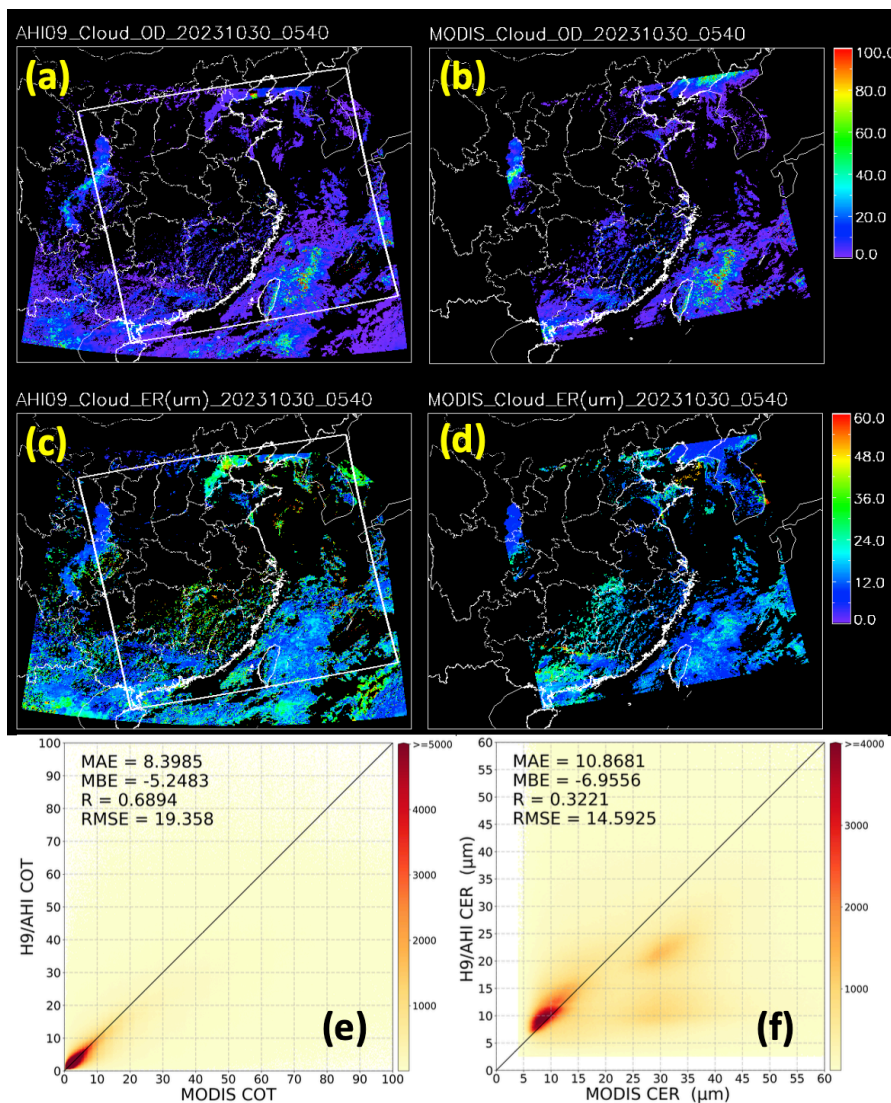


991
992 **Figure 5.** Cloud top height comparisons between (a, c) H9/AHI GEO satellite and (b,
993 d) MODIS at 18:50 UTC (top panel) on October 8, 2023 and 04:30 UTC (bottom panel)
994 on July 10, 2023.

995
996
997
998
999
1000
1001
1002
1003
1004
1005
1006
1007
1008
1009



1010



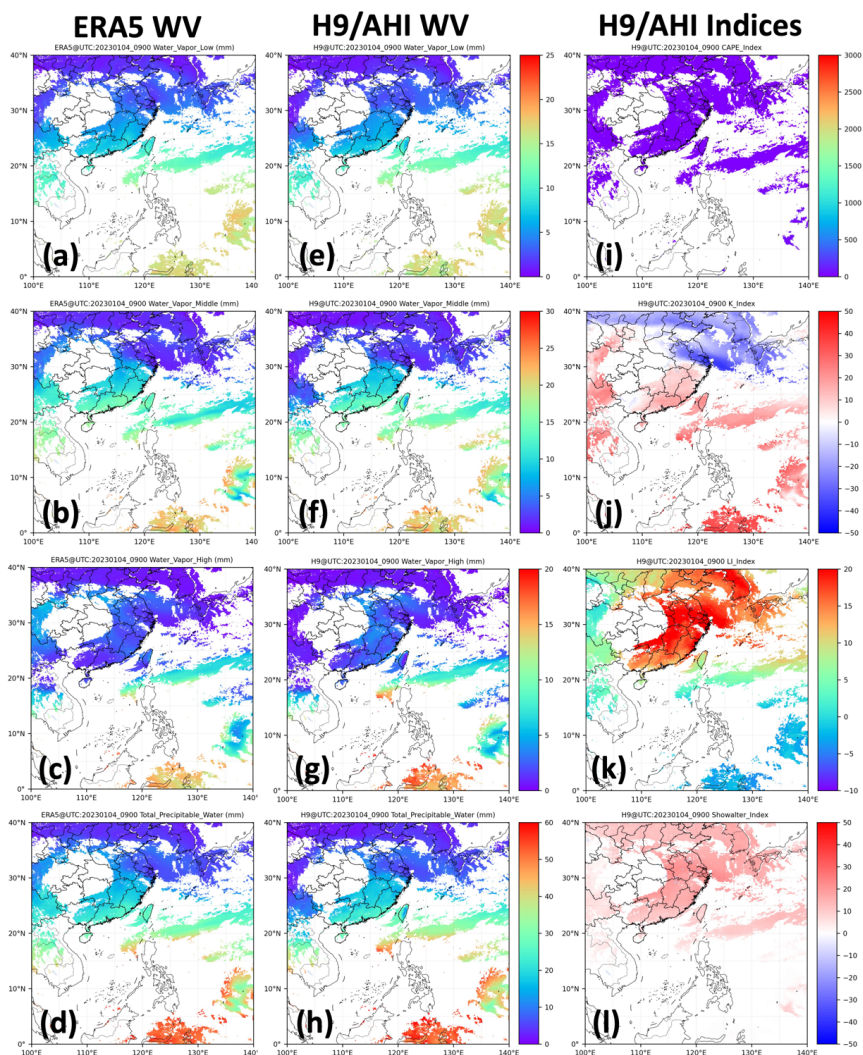
1011

1012 **Figure 6.** Cloud optical depth (top panel) and effective radius (middle panel)
1013 comparisons between (a, c) H9/AHI GEO satellite and (b, d) MODIS at 05:40 UTC on
1014 October 30, 2023. Comparisons of the four months (January, April, July, and October
1015 of 2023) (e) cloud optical depth and (f) effective radius from MODIS and H9/AHI data
1016 over the SCS. The color bar represents the total number in every bin at an interval of
1017 0.2 of COT or 0.2 μm of CER.

1018



1019



1020

1021 **Figure 7.** ERA5 (first column panel) and H9/AHI GEO satellite (middle column panel)

1022 atmospheric (a, e) water vapor at low layer (Surface-900hPa), (b, f) water vapor at

1023 middle layer (900-700hPa), (c, g) water vapor at high layer (700-300hPa), (d, h) total

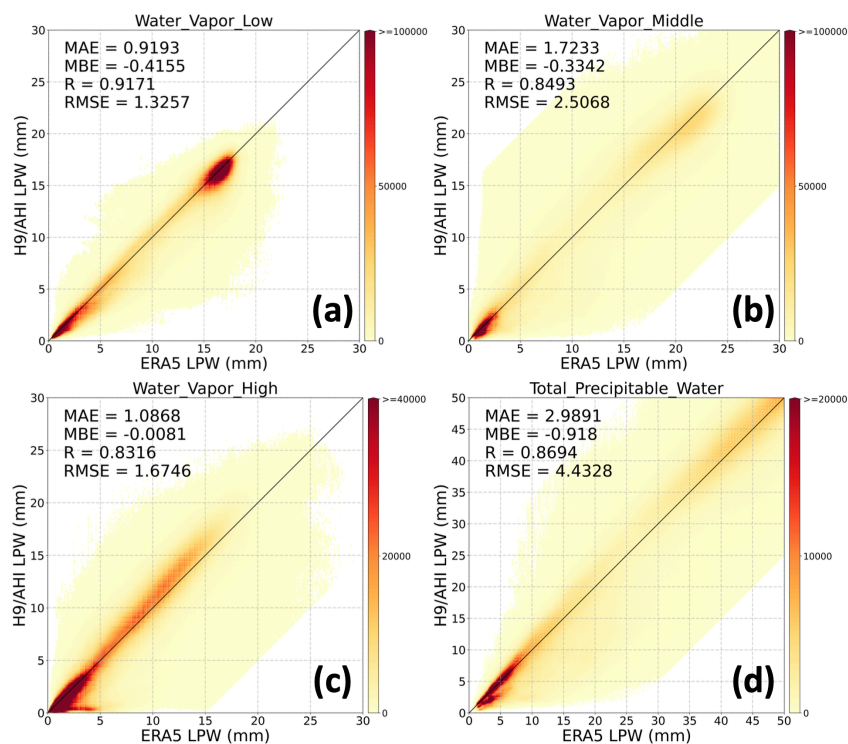
1024 precipitable water, (i) H9/AHI CAPE index, (j) H9/AHI K index, (k) H9/AHI LI index,

1025 and (l) H9/AHI Showalter index at 09:00 UTC on January 4, 2023 over the SCS.

1026



1027



1028

1029 **Figure 8.** Comparisons of the four months (January, April, July, and October of 2023)
1030 layered precipitable water (LPW) values (a, Low; b, Middle; c, High; d, Total) from
1031 ERA5 reanalysis and H9/AHI data over the SCS. The color bar represents the total
1032 number in every bin at an interval of 0.1 mm.

1033

1034

1035

1036

1037

1038

1039

1040

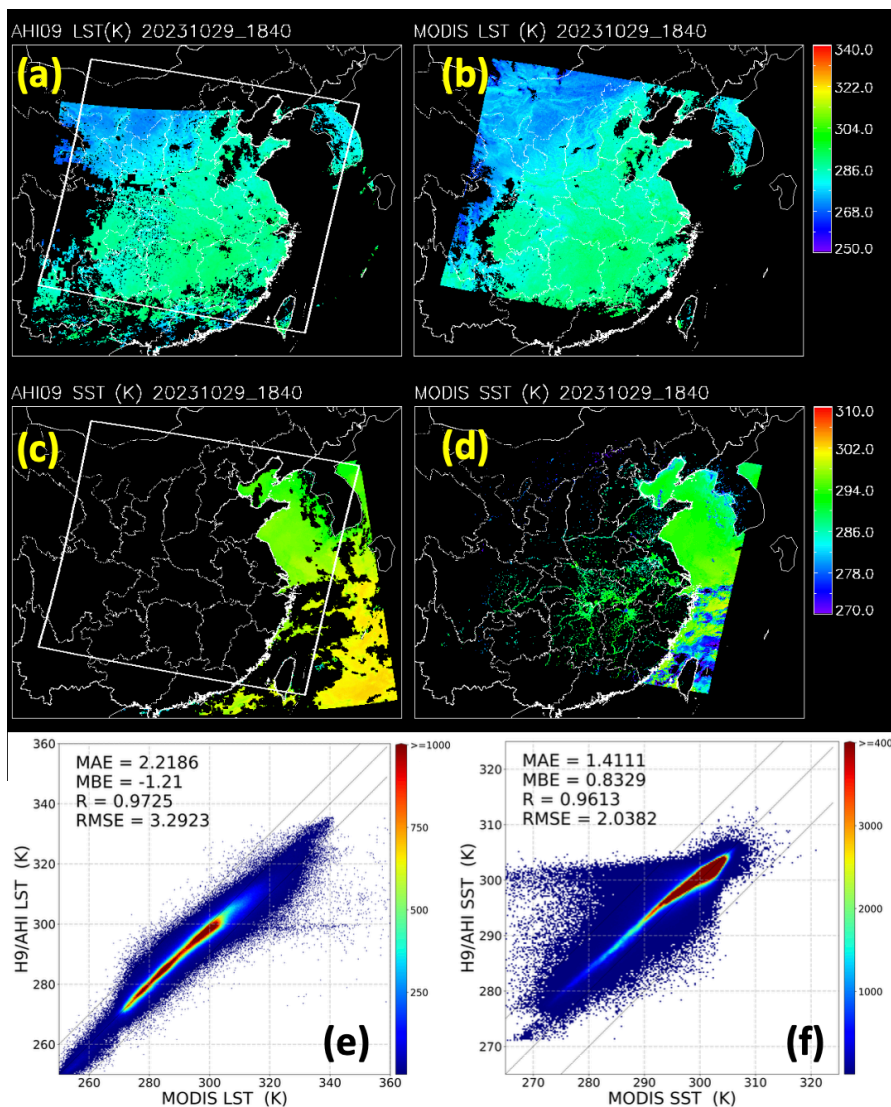
1041

1042

1043



1044



1045

1046 **Figure 9.** LST (top panel) and SST (middle panel) comparisons between (a, c) H9/AHI
1047 GEO satellite and (b, d) MODIS at 18:40 UTC on October 29, 2023. Comparisons of
1048 the four months (January, April, July, and October of 2023) (e) LST and (f) SST from
1049 MODIS and H9/AHI data over the SCS. The color bar represents the total number in
1050 every bin at an interval of 0.25 K of LST or SST.

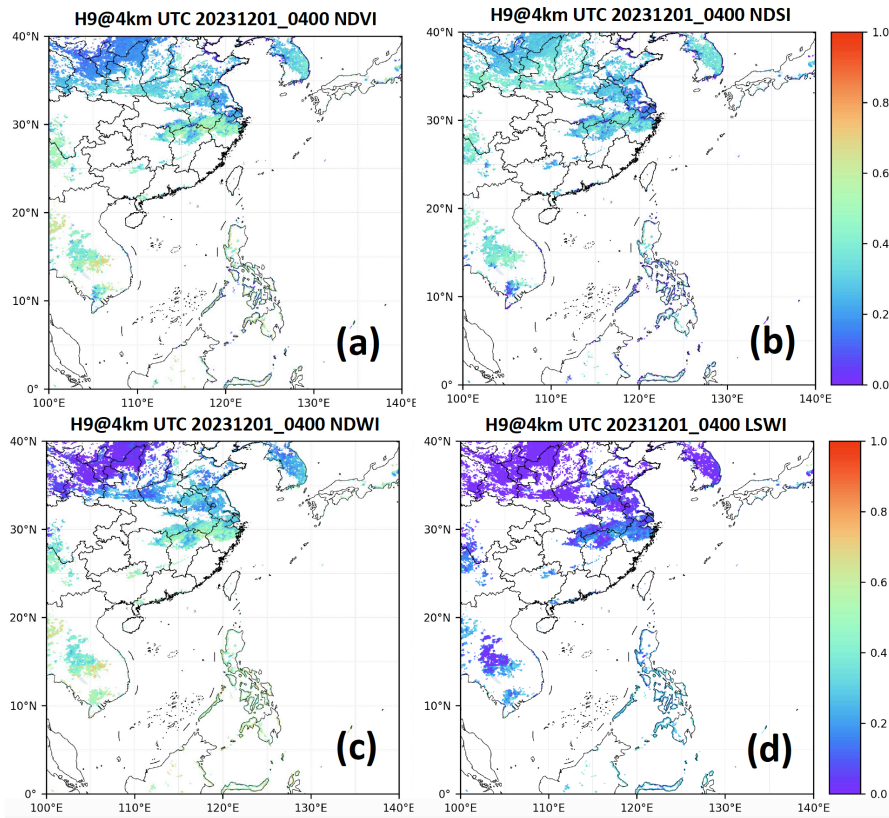
1051

1052



1053

1054



1055

1056 **Figure 10.** (a) NDVI, (b) NDSI, (c) NDWI, and (d) LSWI maps retrieved by H9/AHI

1057 at 04:00 UTC on December 1, 2023 over the SCS.

1058